Sediment mass movement of a particle-laden turbidity current based on ultrasound velocity profiling and the distribution of sediment concentration

SHUN NOMURA[1,2]*, JUMPEI HITOMI[1,3], GIOVANNI DE CESARE[1], YASUSHI TAKEDA[4], YUZURU YAMAMOTO[2] & HIDE SAKAGUCHI[2]

[1]*Laboratoire de Constructions Hydrauliques, EPFL, Lausanne, Switzerland*

[2]*Mathematical Science and Advanced Technology, Japan Agency for Marine-Earth Science and Technology (JAMSTEC), Yokohama, Japan*

[3]*Laboratory for Flow Control, Hokkaido University, Sapporo, Japan*

[4]*Laboratory of Food Process Engineering, ETH, Zurich, Switzerland*

S.N., 0000-0001-5157-7609

**Correspondence: nomura.shun@jamstec.go.jp*

Abstract: Particle-laden flows or turbidity currents along the seafloor are important to the formation and erosion of submarine topography. To understand the mass-transport process, flume tests were carried out with a continuous supply of quartz-laden suspension. The vertical and horizontal velocities were extracted by two pairs of ultrasound Doppler velocity profilers installed at different angles with respect to the bed-normal direction. Due to the head intrusion into the ambient water, the sediment in the suspension was continuously lifted up and mixed, leaving lobes and clefts. The velocity-maximum layer acted as the main sediment conveyor and divided the body into wall and jet regions. The concentration distribution was also quantified based on the relationship between the fluid density and the intensity of light attenuation obtained using a video recording. An area of high sediment concentration was observed just behind the head frontal area. Analysis of the velocity and concentration distribution demonstrated that sediment in the turbidity current was transported mainly by head movement and that continuous sedimentation took place in the wall region. The results indicate that a turbidity current proceeds while maintaining an ordered inner dynamic structure.

Turbidity currents and their deposits have been of research interest where industrial safety and environmental protection are relevant, such as loss of storage capacity in reservoirs or potential for damage to marine infrastructure (Simpson 1997; Mulder & Alexander 2001; Schleiss *et al.* 2016). The velocity structure of such currents and the distribution of sediment concentration in the flow are important to comprehend the sediment transport system and its effect on submarine topography.

Many field observations have provided insight into the sediment transport by turbidity currents despite the difficulties in predicting turbidity currents and in installing monitoring equipment in deep water (e.g. Xu *et al.* 2004, 2010, 2014; Meiburg & Kneller 2010; Mensa *et al.* 2013; Sumner & Paull 2014 and references therein). Several studies have used a combination of flume experiments and numerical models to investigate sediment transport by turbidity currents. Parker *et al.* (1986, 1987) observed the vertical distribution of downstream velocity and sediment concentration. Fukushima *et al.* (1985) explained a basic flow and sediment transfer system by applying the principle of mass conservation in the downstream area, using the depth-averaged method. They concluded that self-acceleration was essential for massive sediment transport and long-term flow continuation, and also described the flow and bedform conditions necessary for self-acceleration. Hartel *et al.* (1997, 2000) and Necker *et al.* (2002) examined the intrusion of a gravity current into ambient water and observed mixing in the head by using a highly resolved three-dimensional direct numerical simulation. Nasr-Azadani & Meiburg (2011, 2013*a*, *b*) and Nasr-Azadani *et al.* (2018) demonstrated the development of lobes and billows induced by instabilities in the foremost area, and observed an entrainment point of diluted suspension in the rear of the head. The development of non-intrusive techniques for measuring velocity or concentration has allowed quantification of the turbulence structure (Kneller & Buckee 2000; Best

From: Lintern, D. G., Mosher, D. C., Moscardelli, L. G., Bobrowsky, P. T., Campbell, C., Chaytor, J. D., Clague, J. J., Georgiopoulou, A., Lajeunesse, P., Normandeau, A., Piper, D. J. W., Scherwath, M., Stacey, C. & Turmel, D. (eds) *Subaqueous Mass Movements*. Geological Society, London, Special Publications, **477**, https://doi.org/10.1144/SP477.19

et al. 2001) and concentration distribution (Nogueira *et al.* 2013, 2014; Theiler & Franca 2016). There exists significant experimental evidence that the flow field and the concentration profile dominate the sediment-transport process. For example, McCaffrey *et al.* (2003) and Choux *et al.* (2005) examined the velocity and concentration distribution through simultaneous measurements using an ultrasound Doppler velocity profiler (UVP) and suspension sampling in a particle-laden flow. Nogueira *et al.* (2013, 2014) developed an image-analysis technique that yields the concentration distribution based on variations in light-attenuation intensity caused by changes in the mass density of the suspension. Theiler & Franca (2016) also confirmed spatio-temporal density development using the same methodology as Nogueira *et al.* (2013, 2014).

As mentioned by Baas *et al.* (2005), the sediment mass-transport system is complicated by the profusion of flow factors and material properties such as velocity distribution, bed form, slope gradient, particle volume fraction and particle size distribution. Indeed, one of the reasons for the incomplete understanding of the sediment mass-transport system is the lack of knowledge of the locally occurring dynamics between the particle-laden fluid and the ambient water (e.g. Kneller *et al.* 1997, 1999, 2016; McCaffrey *et al.* 2003; Gray *et al.* 2005, 2006; Meiburg & Kneller 2010).

In this study, two-dimensional velocity information and concentration distribution were extracted based on two pairs of crossed UVPs and image analysis. We conclude that sediment transport is greatest just behind the head front, continuous sediment transport takes place near the velocity maximum in the body and sedimentation occurs in the wall region, which is just below the velocity maximum.

Facilities and experimental procedure

The experiments were carried out at the Laboratory of Hydraulic Constructions of the École Polytechnique Fédérale de Lausanne (EPFL), Lausanne, Switzerland. The experimental set-up and the coordinate definition are illustrated in Figure 1. The coordinate origin is defined to be at the bottom of the discharge gate. The flume consists of a main tank (dimensions given as width × depth × length: 275 × 980 × 6700 mm), a head tank (275 × 980 × 800 mm) and a mixing tank (600 × 600 × 2400 mm). The main and head tanks are tilted at a slope of 2.4°. The sediment material was quartz flour composed of SiO_2 with a mass density of $\rho_s = 2650$ kg m^{-3}. Its grain sizes at D_{10}, D_{50} and D_{90} are 2.6, 12.2 and 33.0 μm, and the settling velocities (v_s) based on Stokes' law for those sizes are 0.006, 0.133 and 0.978 mm s^{-1}, respectively. A photograph of the quartz flour and a graph of its size distribution are shown in Figure 2. To keep the particles suspended in the head and mixing tank, they were continuously mixed by electric mixers and the particle concentration was intermittently confirmed by a density measurement device (DM-250.1) before and during the experiment. Once the suspension had been well mixed to 2.0 ± 0.05% by volume (i.e. $\rho = 1032$ kg m^{-3}) in the mixing and head tanks, the particle-laden suspension was released by opening a discharge gate to a height of 45.0 mm and simultaneously closing the return pipe. To reproduce the quasi-steady turbidity current, the particle-laden suspension was fed continuously through the gate with a discharge rate of 1.00 l s^{-1}. Counterflow and excessive ambient water trailing, which are usually observed in a lock-exchange configuration (e.g. Kneller *et al.* 1997, 1999; Nogueira *et al.* 2013, 2014; Theiler & Franca

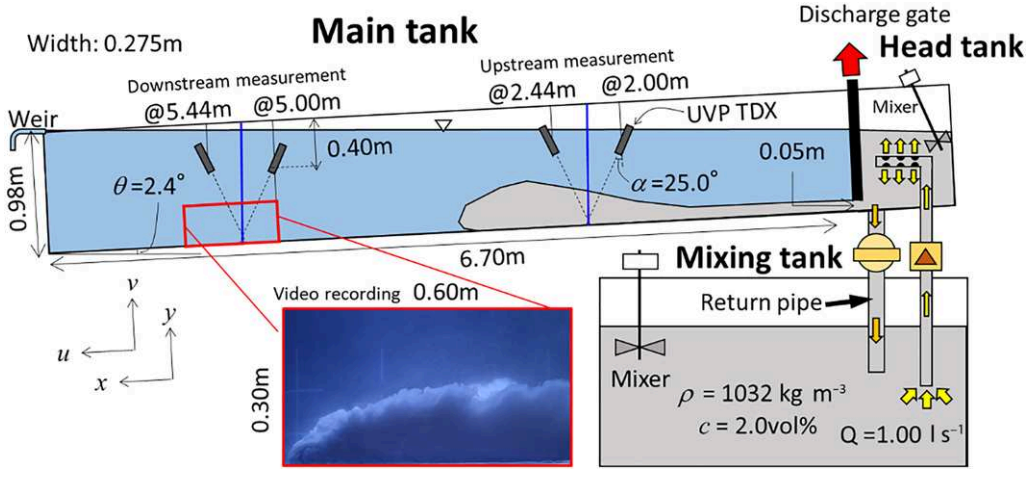

Fig. 1. Schematic view of the flume employed for the experiment using a continuous supply of quartz-laden fluid.

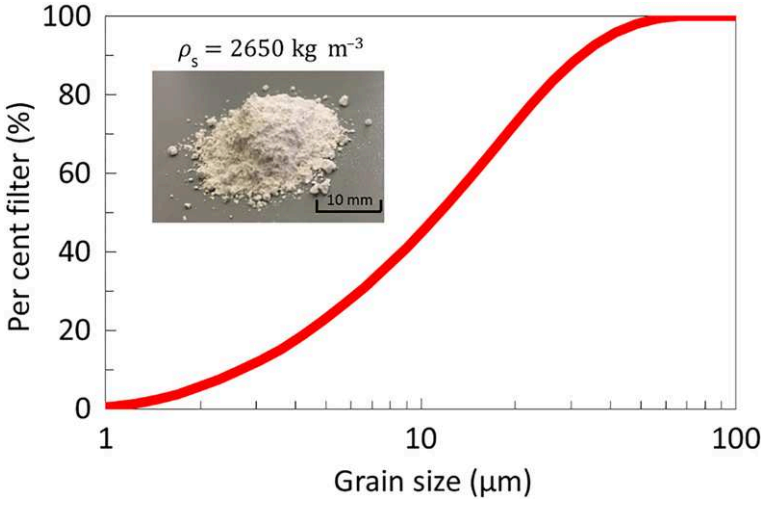

Fig. 2. Photograph and grain-size distribution of the quartz flour used in the experiment.

2016), were not observed at the water surface because the height of the ambient water was sufficiently large relative to the height of the produced turbidity current. To avoid reflection or stagnation effects caused by the end of the wall, the experiment was continued for 100 s after opening the gate, before the head front had reached the end of the flume. More precise details of the experimental set-up can be found in Oehy & Schleiss (2007), Oehy *et al.* (2010) and Chamoun *et al.* (2017). The experiment was performed twice to confirm that an identical flow was produced each time. Although there were differences due to high instability resulting from the turbulence, similar flows were produced in both runs.

For the velocity measurement, two pairs of 4 MHz UVP transducers were installed at $x = 2.00$, 2.44, 5.00 and 5.44 m at an inclination of 25° from the y-axis (Fig. 1). Using two UVP-Duo devices (Met-Flow, Switzerland), the individual UVP measurements in the upstream and downstream areas were obtained as follows. Before flow arrival at $x = 1.50$ m, the upstream measurements ($x = 2.00$ and 2.44 m) were initiated simultaneously for a period of 24 s by an external trigger, after which measurement automatically moved to the downstream measuring points ($x = 5.00$ and 5.44 m) for 24 s. The measurement lines of two pairs of transducers crossed at $(x_c, y_c) = (2.22, 0.10)$ and $(5.22, 0.10)$, which was almost half the height of the flow. This configuration enabled us to extract the velocity information with high spatial resolution (0.67 mm on the y-axis) and to approximate the velocity along the y-axis as u and v at $x = 2.22$ and 5.22 m by applying the temporal velocity conversion based on Taylor's frozen hypothesis. The profile of one measurement element consisted of 64 repeated measurements. A single measurement along the ultrasound beam was completed in 125 ms (i.e. 8.0 Hz). The UVP measurement parameters are listed in Table 1.

A digital camera (D5500, Nikon, Japan) with a single-focus lens (Ai AF Nikkor 50 mm F1.4, Nikon, Japan) was placed 0.50 m from the flume to record the flow at $5.00 \leq x \leq 5.60$ and $0.00 \leq y \leq 0.30$ at a rate of 25 frames/s for image analysis. Here the image resolution is 0.31×0.31 mm/pixel.

Due to the well-controlled continuous suspension release, the flow proceeded with a constant front velocity of $v_f = 100.7$ mm s^{-1} and a flow thickness of $H_f = 170$ mm. The flow Reynolds number was $\mathrm{Re} = v_f H_f/\nu = 1.71 \times 10^4$ and the densimetric Froude number was $\mathrm{Fr}' = v_f[gH_f(\rho - \rho_w)/\rho]^{-0.5} = 0.43$, where g is acceleration due to gravity (9.80 m s^{-2})

Table 1. *Main parameters of UVP measurement*

Parameter	Value
Ultrasound frequency (Hz)	4 M
Ultrasound velocity (m s^{-1})	1480
Maximum velocity (mm s^{-1})	±90.6
Velocity resolution (mm s^{-1})	0.713
Measuring window (mm)	0.37–747.77
Number of channels	1011
Number of profiles	990
Sampling period for each profile (ms)	125
Window start (mm)	0.37
Window end (mm)	747.77
Channel distance(mm)	0.74
Channel width (mm)	0.74
Pulse repetition frequency (Hz)	986.7
Frequency (Hz)	8.00

and ρ_w is the mass density of ambient water (1000 kg m^{-3}). The flow was fully turbulent and subcritical according to Parker *et al.* (1986) and Kneller *et al.* (1999).

Methodology

Velocity structure

At the crossing point of the two measurement lines of individual UVP, the u and v components are represented as follows (Takeda 2012):

$$u = \frac{u_1 - u_2}{2\sin\alpha} \tag{1}$$

$$v = -\frac{u_1 + u_2}{2\cos\alpha} \tag{2}$$

where u_1 and u_2 are the velocities directly measured by an upstream and a downstream UVP, respectively, and α is the acute angle from the y-axis. The inclined velocity components can be transformed assuming that the rate of change of velocity within the flow is small compared with the representative flow velocity (Kneller *et al.* 1999). Adapting v_f as a representative velocity and defining the time lag dT due to the inclination of measurement lines from bed-normal, the time t at $x = x_c$ is corrected as follows:

$$t = t' + \mathrm{d}T = t' + \frac{(S - s)\sin\alpha}{v_f} \tag{3}$$

where t' is the original measurement time, s is the distance from the bottom to (x_c, y_c) along the measurement line and S is the distance from the bottom to the target along the measurement line, expressed as:

$$y = S\cos\ \alpha. \tag{4}$$

Using equations (3) and (4), u_1 and u_2 are arranged in the bed-normal direction. Then, u and v for any t and y at $x = 2.22$ and 5.22 m are derived from equations (1) and (2), respectively. Here the maximum absolute value of dT (0.46 s) is observed at $y =$ 0.00 m, which is less than the duration of four profiles and is small enough to conclude that u and v can be transformed in the present experimental set-up.

Divergence, vorticity and stream function

To discuss the flow structure, the divergence (div$\boldsymbol{v}$) and vorticity (ω) were evaluated as follows:

$$\mathrm{div}\boldsymbol{v} = \frac{\mathrm{d}\bar{u}}{\mathrm{d}x} + \frac{\mathrm{d}\bar{v}}{\mathrm{d}y} \tag{5}$$

$$\omega = \frac{\mathrm{d}\bar{v}}{\mathrm{d}x} - \frac{\mathrm{d}\bar{u}}{\mathrm{d}y} \tag{6}$$

where dx is defined as the product of dt and v_f (dx = dt v_f = 12.6 mm) and dy = 7.4 mm. The average depth value (dy) is adopted for $\bar{u}$ and $\bar{v}$ to reduce the noise in the original measurement. Positive and negative values of div$\boldsymbol{v}$ indicate outwards and inwards flow, respectively; positive and negative values of ω denote anticlockwise and clockwise flow, respectively.

To discuss the stream line, the stream function, Ψ, is employed, as follows:

$$\Psi = \int_0^y \bar{u}\,\mathrm{d}y. \tag{7}$$

The counter line of Ψ (i.e. Ψ = const.) defines the stream line for the case of two-dimensional incompressible flow.

Concentration distribution

For the concentration distribution, Nogueira *et al.* (2013, 2014) and Theiler & Franca (2016) used the relationship between the suspension density and a greyscale image. The concentration–greyscale relationship was initially calibrated from images of the particle-laden suspension up to $c = 2.00\%$ under controlled lighting conditions. Subsequently, the concentration distribution of the turbidity current was defined from the recorded image and the obtained relationship.

Experimental results

Velocity distribution

Figure 3 shows the distribution of u and v at $x = 2.22$ and 5.22 m for 20 s from 2 s before the flow arrival. The head is characterized by an abrupt increase in u up to $y = H_f$ with a specific gradient. The positive v along the head slope represents lifting of the ambient water by the flow intrusion, and the downwards v that appears after passing the highest part of the head is related to recirculation of the suspension into the head. The body is recognized as the relatively steady area following the head (Baas *et al.* 2005). Although there are no clear boundaries to divide the head and the body due to the instability of the transition process, the body arrives from at least $t = 10$ s; consequently, we define body initiation at $t = 10$ s. The time-averaged maximum streamwise velocity, u_{max}, of the body is observed at $y = 34$ and 32 mm as $u_{max} = 165.0$ and 88.0 mm s^{-1} at $x =$ 2.22 and 5.22 m, respectively. As reported by Altinaker *et al.* (1996), Baas *et al.* (2005) and Xu (2010), among others, a velocity maximum divides the profile into a wall region (WR) below the maximum and a jet region (JR) above the maximum. A pair of negative and positive v is present around the upper interface with the ambient water due to

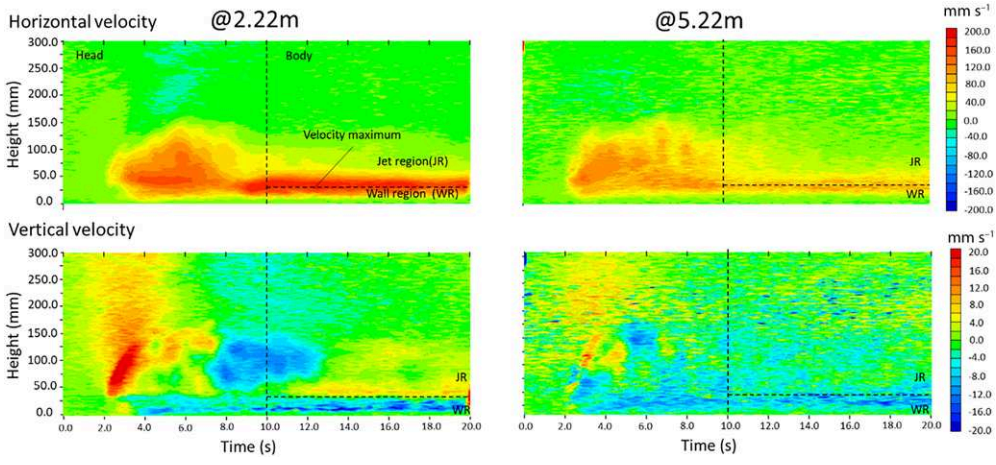

Fig. 3. Spatial and temporal velocity distribution of u (upper part of the figure) and v (lower part of the figure) at x = 2.22 (left) and 5.22 m (right). Vertical and horizontal dashed lines represent the boundary of the head and body, and the horizontal velocity maximum.

the intrusion and passing of the head. The positive and negative v layers are also clearly observed at $x = 2.22$ m in the JR and WR, while negative v is observed in the JR at $x = 5.22$ m. Comparing the results at $x = 2.22$ and 5.22 m, the velocity structures in the head and body maintain a similar geometry by means of constant finite-volume suspension discharge, although the velocity is attenuated.

Divergence and vorticity distribution

The vorticity and divergence distribution obtained using equations (5) and (6) are presented in Figure 4.

Along the upper contour of the head, negative div$\boldsymbol{v}$ and ω are developed, and ω is gradually attenuated with time. In the WR, negative div$\boldsymbol{v}$ and positive ω layers are clearly observed; in the JR, there are positive div$\boldsymbol{v}$ and negative ω layers. In the div$\boldsymbol{v}$ distribution, these layers are derived mainly from the vertical gradient of v because the fluctuation in u with time is relatively weak, resulting in two horizontal layers being present in the div$\boldsymbol{v}$ distribution. In addition, the gradient of u in the vertical direction is pronounced due to shear resistance from the static ambient water and the flume bottom. As a result, two well-stratified layers are clearly observed in the WR and JR.

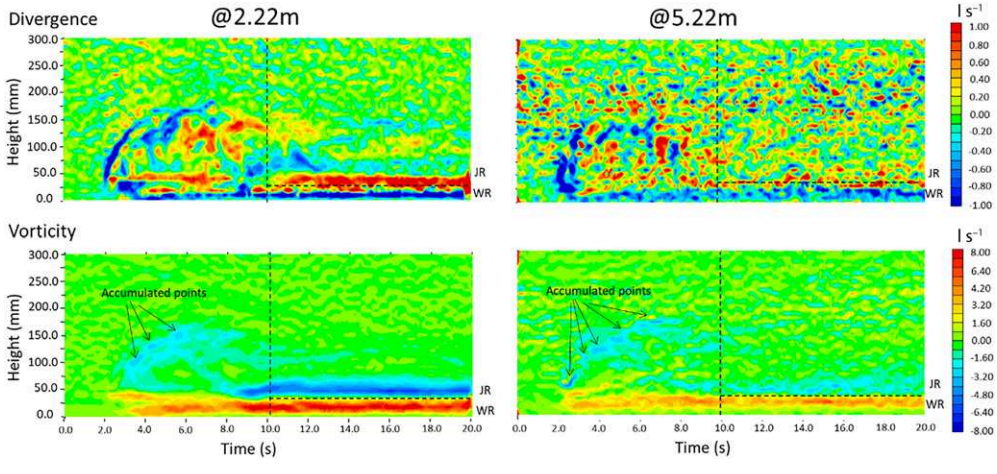

Fig. 4. Spatial and temporal divergence (upper part of the figure) and vorticity (lower part of the figure) distribution at x = 2.22 (left) and 5.22 m (right). Vertical and horizontal dashed lines represent the boundary of the head and body, and the horizontal velocity maximum.

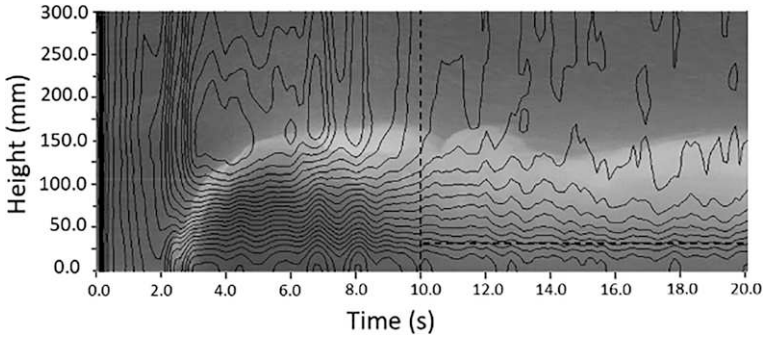

Fig. 5. Timeline image and equipotential lines at $x = 5.22$ m. One pixel corresponds to 0.04 s × 0.31 mm. Vertical and horizontal dashed lines represent the boundary of the head and body, and the horizontal velocity maximum.

Timeline image and stream function

Figure 5 shows a timeline image extracted from the recorded video and the distribution of $\Psi = \text{const.}$ obtained using equation (7). The timeline image was made by extracting the images at $x = 5.22$ m and arranging them according to the time direction. As a result of the intrusion of the flow, the suspension is lifted up along the interface with the ambient water; subsequently, the effect weakens as the head passes. The closed lines of $\Psi = \text{const.}$ observed above the frontal interface indicate that the suspension is mixed with the ambient water and supplied again after dilution. The lines of $\Psi = \text{const.}$ are distributed horizontally up to $y = 100$ mm in the body, which indicates that the suspension is continuously supplied from the body to the foremost part of the flow without mixing with the ambient water.

Concentration distribution

By applying the image analysis to Figure 5, the concentration distribution is extracted, as shown in Figure 6. Here, the concentration is the ratio of sediment volume normalized to the total volume (i.e. the volume fraction). Just behind the head front, suspended sediment accumulates due to the continuous supply of suspended sediment from the body, although its maximum value is reduced to half that of the original discharge ($c = 0.02$) because of sedimentation and mixing with the ambient water. The concentration abruptly increases as a result of flow arrival and gradually decreases at all depths in the head. After the head has passed, a diluted suspension that remains horizontally static is observed as a residual of the suspended sediment.

Sediment mass flux

Figure 7 shows the products of velocity and concentration, cu and cv, at $x = 5.22$ m (i.e. the sediment mass-flux distribution). As the space–time resolution was low in the velocity distribution (resolution of 0.67 mm × 0.125 ms: Fig. 3), the concentration profile (resolution of 0.31 mm × 0.04 ms: Fig. 6) was redrawn at the same resolution. As the area of high sediment concentration is located in the head, the intensity of the sediment mass flux is also high. Large amounts of sediment are carried in the downstream direction in the head due to the accumulated

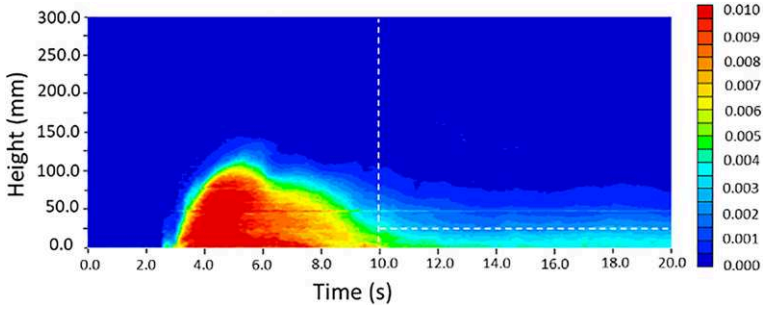

Fig. 6. Concentration distribution at $x = 5.22$ m. Vertical and horizontal dashed lines represent the boundary of the head and body, and the horizontal velocity maximum.

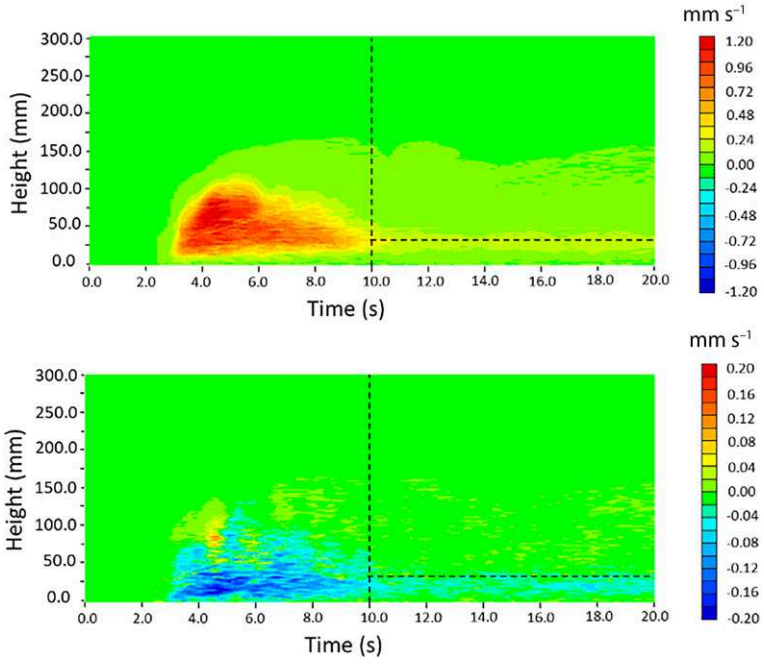

Fig. 7. Sediment mass flux in the streamwise direction (upper part of the figure) and the vertical direction (lower part of the figure) at $x = 5.22$ m. Vertical and horizontal dashed lines represent the boundary of the head and body, and the horizontal velocity maximum.

concentration and high velocity. Reflecting the negative v, negative cv is developed mainly in the head and the WR.

Discussion

Flow structure in the head and interface with the ambient water

In the foremost part of the flow, negative divergence and vorticity are developed (Fig. 4), indicating that the suspension is contracted at that point. Then an uplift flow is generated at the interface with the ambient water (Figs 3 & 5), leaving a clockwise rotation (i.e. negative ω). The distribution of ω along the frontal interface represents several accumulated points, implying that the specific lobe and cleft morphology is continuously generated with time. The suspension that reached the highest part of the area is released from that point with negative v and decreasing u, and is entrained as recirculation flow (Figs 3 & 5); however, the sediment mass flux is not relevant for $y > 100$ mm due to the low concentration in that area (Figs 6 & 7). Kneller *et al.* (1999) described how a Kelvin–Helmholtz instability would be developed along the upper horizontal interface with the ambient water as a result of the unstable shear after the head has passed. Such shearing processes cause a substantial consumption of momentum without downstream sediment transport.

Flow structure in the body

In the body, u_{max} is observed at a height of about 20% of the total height ($= y_{u_{max}}/H_f$) as a result of friction with the rigid bottom and trailing of the flow by static water. This velocity maximum divides the area into the WR and JR (Figs 3 & 4). At $x = 2.22$ m, negative v is constantly observed in the WR and positive v is represented in the JR, as described by Gray *et al.* (2005). These results suggest that the suspension in the velocity maximum proceeds downstream while the suspension is separated vertically by the intrusion of the maximum velocity flow. Although the absolute value of v is five times less than that of u_{max}, it is 10 times greater than the value of v_s for D_{50}, indicating that both static particle setting and substantial downwards flow are pronounced in this area. As the UVPs are installed in the centre of the spinwise direction, it is difficult to discuss the flow in that direction; however, it is possible that secondary flow in the spinwise direction would be generated to satisfy the mass conservation of sediment.

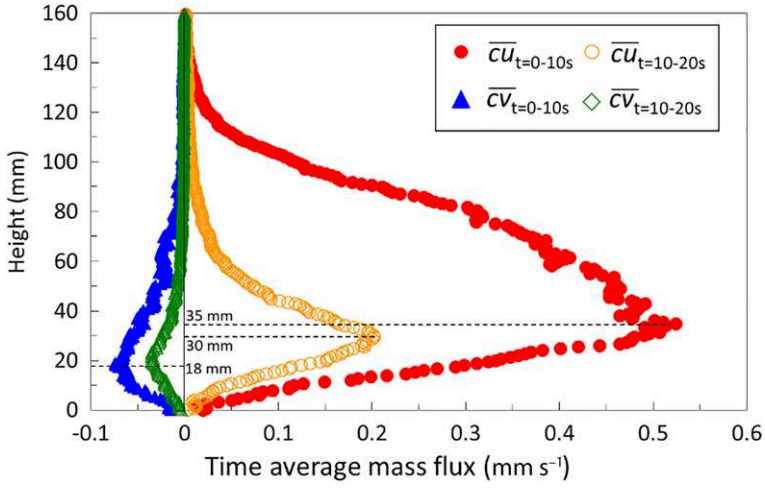

Fig. 8. Time-averaged sediment mass flux distribution at t = 0–10 and 10–20 s at x = 5.22 m.

Sediment mass flux in the head and body

The average sediment mass flux in the x and y directions for every 10 s ($\overline{cu}$ and $\overline{cv}$) is shown in Figure 8. The plots have a vertically convex shape converging to 0 at the bottom and at the upper interface with the ambient water due to the 0 values of velocity and concentration, respectively. The absolute values for t = 0–10 s are larger than those for t = 10–20 s at all heights, which means that the head is dominant in conveying the suspended sediment. For t = 0–10 s, $\overline{cu}$ is well developed at y = 60–120 mm, where the head slope by the intrusion is observed, resulting in the height of the maximum observed $\overline{cu}$ (y = 35 mm) being higher than that of $\overline{cu}$ at t = 10–20 s. In the body, u is also high around the velocity maximum; however, the suspension concentration is substantially reduced and the mass flux becomes smaller than in the head.

As shown in Figure 3, v at x = 5.22 m has a negative value as a result of recirculation flow to the head, flow separation in the body and constant static settling; thus, negative $\overline{cv}$ is observed in the vertical direction. As the observed velocity and concentration are high in the head, the intensity of $\overline{cv}$ is also high in that region (Fig. 8); however, the plot distribution forms are similar in both areas and the maximum intensity is located at the same height (y = 18 mm), implying that sediment transfer occurs in a similar manner despite the intensity difference.

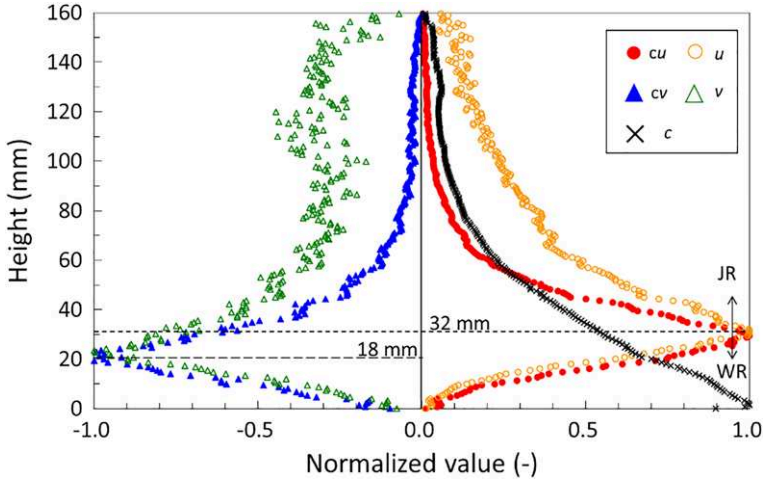

Fig. 9. Normalized sediment mass flux, velocity and concentration distribution at t = 0–10 and 10–20 s at x = 5.22 m.

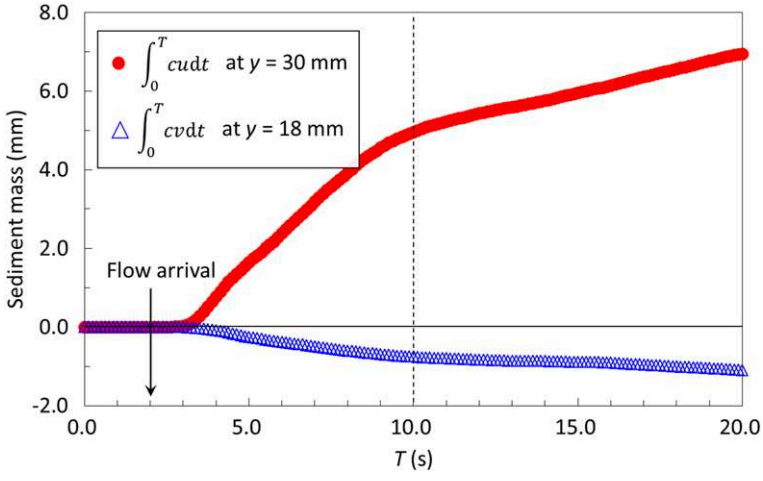

Fig. 10. Time-integrated sediment mass flux for u and v at $y = 30$ and 18 mm.

The ratio of the mass flux in both directions at 10 s intervals ($=\overline{cu}/\overline{cv}$) is -10.7 for $t = 0$–10 s and -6.0 for $t = 10$–20 s, indicating that the transportation in the streamwise direction is more pronounced than sedimentation in the head and body.

The sediment mass flux, velocity and concentration normalized by the maximum absolute value of each variable for $t = 10$–20 s are shown in Figure 9. The curves of sediment mass flux and velocity are convex, and the concentration shows an increase towards the bottom. The peak values of sediment mass flux and velocity in both directions are located at similar heights ($y = 30$ and 18 mm), respectively. Here, the peak height of cv is situated in the WR, suggesting that the suspension located below u_{max} is carried downwards during the streamwise transport in that area. The time integrations of cu and cv at their peak heights are plotted in Figure 10. When the flow arrives ($t = 2$ s), the integration of mass flux starts increasing (decreasing) in the x (y) direction with time. After $t = 10$ s, corresponding to the initiation of the body, the absolute gradients decrease in both areas. The gradients for 3–10 and 10–20 s are 0.705 and 0.200 mm s^{-1} horizontally, respectively, and -0.107 and -0.034 mm s^{-1} vertically, respectively, confirming that a substantial amount of sediment is conveyed downstream in the head, and a small but constant quantity of sediment is transported by u_{max} during sedimentation.

Conclusions

We observed the temporal development of velocity and sediment concentration in an experimentally produced particle-laden turbidity current by using two pairs of UVPs and image analysis from video recordings. The vorticity and divergence distributions were extracted from the velocity distribution. Analysis of spatio-temporal trends in velocity, divergence and vorticity structure yielded the following results: (1) the suspension along the foremost interface with the ambient water is lifted up, leaving lobes and clefts induced by instability caused by the head intrusion; (2) the maximum streamwise velocity, u_{max}, is observed at 20% of the total flow height in the body and divides the body into a wall region (WR) and a jet region (JR); and (3) negative (positive) v is generated in the WR (JR) as a result of the flow separation by the velocity maximum, and negative v causes substantial sedimentation. These fundamental velocity structures are preserved in the streamwise direction, although their intensity is attenuated by continuous kinetic energy consumption and particle diffusion or sedimentation, implying that an extra energy supply is essential for continued movement of the particle-laden turbidity current. The distribution of sediment concentration obtained from image analysis demonstrates that the accumulated suspension is located behind the head. In the body, the sediment concentration is vertically homogenous due to the steady velocity distribution. As a result of the velocity and concentration distributions, large amounts of sediment are carried by the head because of the accumulation of sediment in the streamwise direction, whereas constant amounts of sediment are carried by the body. The presence of the vertical sediment mass flux induced by v confirms that the WR acts as a potential region of sedimentation and indicates the need to consider the mass flux in the vertical direction, as described by Parker *et al.* (1986). This point will be discussed

further in future studies that include information on the spinwise direction. In the interface, although energy consumption is intense due to mixing by lobes and clefts, and recirculation by entrainment, sediment mass flux is not pronounced around the interface with the ambient water. These insights are in good agreement with the theoretical work of Gray *et al.* (2005), and supplement the numerical results of Bhaganagar (2017) and Nasr-Azadani *et al.* (2018).

Scale effects in time and space are not fully addressed in this work; however, several of the insights presented above will be of use in comprehending turbidity-current dynamics in nature, for the following reasons. (1) Quartz flour is adopted as the sediment; thus, it is possible to discuss the particle–fluid interactions causing sediment and mass transport, energy production, or dissipation. (2) The water in the flume was sufficiently deep that a counterflow and trailing water were not observed in the surface water. (3) The suspension was steadily supplied from the gate without disturbance, meaning that a quasi-steady flow was produced in the flume. In addition, as discussed previously (e.g. Swenson & Muto 2007; Hsu & Capart 2008; Malverti *et al.* 2008), it is possible to extrapolate the flow configuration and sediment transport from the experimental scale to natural turbulent flows, which will help to elucidate scale effects more precisely. In addition to the consideration of such scale effects, a statistical analysis of factors such as Reynolds' stress and turbulent kinematic energy (Kneller *et al.* 1997, 1999; Baas *et al.* 2005; Gray *et al.* 2005, 2006; Verhagen *et al.* 2013) will be carried out as part of future work to comprehend the flow field, sediment conveyer system and momentum transfer process more precisely.

Acknowledgements The authors would like to thank Prof. Y. Murai and Assoc. Prof. Y. Tasaka for their support and helpful comments. We are grateful to Dr S. Chamoun for technical assistance with the experiments.

Funding This work was supported by the JAMSTEC Researcher Overseas Dispatch Budget and a Grant-in-Aid for Young Scientists to S. Nomura (grant No. 15K18115) from the Japan Society for the Promotion of Science.

References

Altinaker, M.S., Graf, W.H. & Hopfinger, E.J. 1996. Flow structure in turbidity currents. *Journal of Hydraulic Research*, **34**, 713–718, https://doi.org/10.1080/00221689609498467

Baas, J.H., McCaffrey, W.D., Haughton, P.D.W. & Choux, C. 2005. Coupling between suspended sediment distribution and turbulence structure in a laboratory turbidity current. *Journal of Geophysical Research*, **110**, C11015, https://doi.org/10.1029/2004JC002668

Best, J.L., Kirkbride, A.D. & Peakall, J. 2001. Mean flow and turbulence structure of sediment-laden gravity currents: new insights using ultrasonic Doppler velocity profiling. *In*: McCaffrey, W., Kneller, B. & Peakall, J. (eds) *Particulate Gravity Currents*. International Association of Sedimentologists, Special Publications, **31**, 159–172, https://doi.org/10.1002/9781444304275.ch12

Bhaganagar, K. 2017. Role of head of turbulent 3-D density currents in mixing during slumping regime. *Physics of Fluids*, **29**, 020703-1-12, https://doi.org/10.1063/1.4974353

Chamoun, S., De Cesare, G. & Schleiss, A.J. 2017. Venting of turbidity currents approaching a rectangular opening on a horizontal bed. *Journal of Hydraulic Research*, 1–15, https://doi.org/10.1080/00221686.2017.1289266

Choux, C., Baas, J.H., McCaffrey, W.D. & Haughton, P.D.W. 2005. Comparison of spatio-temporal evolution of experimental particulate gravity flows at two different initial concentrations, based on velocity, grain size and density data. *Sedimentary Geology*, **179**, 49–69, https://doi.org/10.1016/j.sedgeo.2005.04.010

Fukushima, Y., Parker, G. & Pantin, H.M. 1985. Prediction of ignitive turbidity currents in Scripps Submarine Canyon. *Marine Geology*, **67**, 55–81.

Gray, T.E., Alexander, J. & Leeder, M.R. 2005. Quantifying velocity and turbulence structure in depositing sustained turbidity currents across breaks in slope. *Sedimentology*, **52**, 467–488, https://doi.org/10.1111/j.1365-3091.2005.00705.x

Gray, T.E., Alexander, J. & Leeder, M.R. 2006. Longitudinal flow evolution and turbulence structure of dynamically similar, sustained, saline density and turbidity currents. *Journal of Geophysical Research*, **111**, C08015, https://doi.org/10.1029/2005JC003089

Hartel, C., Kleiser, L., Michaud, M. & Stein, C.F. 1997. A direct numerical simulation approach to the study of intrusion fronts. *Journal of Engineering Mathematics*, **32**, 103–120, https://doi.org/10.1023/A:1004215331070

Hartel, C., Meiburg, E. & Necker, F. 2000. Analysis and direct numerical simulation of the flow at a gravity-current head. 1. Flow topology and front speed for slip and no-slip boundary. *Journal of Fluid Mechanics*, **418**, 189–212, https://doi.org/10.1017/S0022112000001221

Hsu, J.P.C. & Capart, H. 2008. Onset and growth of tributary-dammed lakes. *Water Resources Research*, **44**, W11201, https://doi.org/10.1029/2008WR007020

Kneller, B., Nasr-Azadani, M.M., Radhakrishnan, S. & Meiburg, E. 2016. Long-range sediment transport in the world's oceans by stably stratified turbidity currents. *Journal of Geophysical Research: Oceans*, **121**, 8608–8620, https://doi.org/10.1002/2016JC011978

Kneller, B.C. & Buckee, C. 2000. The structure and fluid mechanics of turbidity currents: a review of some recent studies and their geological implications. *Sedimentology*, **47**, 62–94, https://doi.org/10.1046/j.1365-3091.2000.047s1062.x

Kneller, B.C., Bennett, S.J. & McCaffrey, W.D. 1997. Velocity and turbulence structure of gravity currents and internal solitary waves: potential sediment transport and the formation of wave ripples in deep water. *Sedimentary Geology*, **112**, 235–250, https://doi.org/10.1016/S0037-0738(97)00031-6

Kneller, B.C., Bennett, S.J. & McCaffrey, W.D. 1999. Velocity structure, turbulence and fluid stresses in experimental gravity currents. *Journal of Geophysical Research: Oceans*, **104**, 5381–5391, https://doi.org/10.1029/1998JC900077

Malverti, L., Lajeunesse, E. & Métivier, F. 2008. Small is beautiful: Upscaling from microscale laminar to natural turbulent rivers. *Journal of Geophysical Research: Earth Surface*, **113**, F04004, https://doi.org/10.1029/2007JF000974

McCaffrey, W.D., Choux, C.M.A., Baas, J.H. & Haughton, P.D.W. 2003. Spatio-temporal evolution of velocity structure, concentration and grain size stratification within experimental particulate gravity currents. *Marine and Petroleum Geology*, **20**, 851–860, https://doi.org/10.1016/j.marpetgeo.2003.02.002

Meiburg, E. & Kneller, B. 2010. Turbidity currents and their deposits. *Annual Review of Fluid Mechanics*, **42**, 135–156, https://doi.org/10.1146/annurev-fluid-121108-145618

Mensa, J.A., Garraffo, Z., Griffa, A., Özgökmen, T.M., Haza, A. & Veneziani, M. 2013. Seasonality of the submesoscale dynamics in the Gulf Stream region. *Ocean Dynamics*, **63**, 923–941, https://doi.org/10.1007/s10236-013-0633-1

Mulder, T.M. & Alexander, J. 2001. The physical character of subaqueous sedimentary density flows and their deposits. *Sedimentology*, **48**, 269–299, https://doi.org/10.1046/j.1365-3091.2001.00360.x

Nasr-Azadani, M.M. & Meiburg, E. 2011. TURBINS: an immersed boundary, Navier–Stokes code for the simulation of gravity and turbidity currents interacting with complex topographies. *Computers & Fluids*, **45**, 14–28, https://doi.org/10.1016/j.compfluid.2010.11.023

Nasr-Azadani, M.M. & Meiburg, E. 2013*a*. Polydisperse turbidity currents propagating over complex topography: comparison of experimental and depth-resolved simulation results. *Computers & Geosciences*, **53**, 141–153, https://doi.org/10.1016/j.cageo.2011.08.030

Nasr-Azadani, M.M. & Meiburg, E. 2013*b*. Influence of seafloor topography on the depositional behavior of bi-disperse turbidity currents: a three-dimensional, depth-resolved numerical investigation. *Environmental Fluid Mechanics*, **14**, 319–342, https://doi.org/10.1007/s10652-013-9292-5

Nasr-Azadani, M.M., Meiburg, E. & Kneller, B. 2018. Mixing dynamics of turbidity currents interacting with complex seafloor topography. *Environmental Fluid Mechanics*, **18**, 210–223, https://doi.org/10.1007/s10652-016-9477-9

Necker, F., Hartel, C., Kleiser, L. & Meiburg, E. 2002. High resolution simulations of particle laden gravity currents. *International Journal of Multiphase Flow*, **28**, 279–300, https://doi.org/10.1016/S0301-9322(01)00065-9

Nogueira, H.I.S., Adduce, C., Alves, E. & Franca, M.J. 2013. Image analysis technique applied to lock-exchange gravity currents. *Measurement Science and Technology*, **24**, 047001, https://doi.org/10.1088/0957-0233/24/4/047001

Nogueira, H.I.S., Adduce, C., Alves, E. & Franca, M.J. 2014. Dynamics of the head of gravity currents. *Environmental Fluid Mechanics*, **14**, 519–540, https://doi.org/10.1007/s10652-013-9315-2

Oehy, Ch. & Schleiss, A.J. 2007. Control of turbidity currents in reservoirs by solid and permeable obstacles. *Journal of Hydraulic Engineering*, **133**, 637–648, https://doi.org/10.1061/(ASCE)0733-9429(2007)133:6(637)

Oehy, Ch., De Cesare, G. & Schleiss, A.J. 2010. Effect of inclined jet screen on turbidity current. *Journal of Hydraulic Research*, **48**, 81–90, https://doi.org/10.1080/00221680903566042

Parker, G., Fukushima, Y. & Pantin, H.M. 1986. Self acceleration turbidity currents. *Journal of Fluid Mechanics*, **171**, 145–181.

Parker, G., Garcia, M., Fukushima, M. & Yu, M. 1987. Experiments on turbidity currents over an erodible bed. *Journal of Hydraulic Research*, **25**, 123–147.

Schleiss, A.J., Franca, M.J., Jiménez, C.J. & De Cesare, G. 2016. Reservoir sedimentation. *Journal of Hydraulic Research*, **54**, 595–314, https://doi.org/10.1080/00221686.2016.1225320

Simpson, J.E. 1997. *Gravity Currents: In the Environment and the Laboratory*. Cambridge University Press, London.

Sumner, E.J. & Paull, C.K. 2014. Swept away by a turbidity current in Mendocino submarine canyon, California. *Geophysical Research Letters*, **41**, 7611–7618, https://doi.org/10.1002/2014GL061863

Swenson, J.B. & Muto, T. 2007. Response of coastal plain rivers to falling relative sea-level: allogenic controls on the aggradational phase. *Sedimentology*, **54**, 207–221, https://doi.org/10.1111/j.1365-3091.2006.00830.x

Takeda, Y. 2012. *Ultrasonic Doppler Velocity Profiler for Fluid Flow (Fluid Mechanics and Its Applications)*. Springer, New York.

Theiler, Q. & Franca, M.J. 2016. Contained density currents with high volume of release. *Sedimentology*, **63**, 1820–1842, https://doi.org/10.1111/sed.12295

Verhagen, I.T.E., Baa, J.H., Jacinto, R.S., McCaffrey, W.D. & Davies, A.G. 2013. A first classification scheme of flow-bed interaction for clay-laden density currents and soft substrates. *Ocean Dynamics*, **63**, 385–397, https://doi.org/10.1007/s10236-013-0602-8

Xu, J., Swarzenski, P., Noble, M. & Li, A.C. 2010. Event-driven sediment flux in Hueneme and Mugu submarine canyons, southern California. *Marine Geology*, **269**, 74–88, https://doi.org/10.1016/j.margeo.2009.12.007

Xu, J., Sequeiros, O. & Noble, M. 2014. Sediment concentrations, flow conditions, and downstream evolution of two turbidity currents, Monterey Canyon, USA, Deep Sea Research Part I. *Ocean Research*, **89**, 11–34, https://doi.org/10.1016/j.dsr.2014.04.001

Xu, J.P. 2010. Normalized velocity profiles of field-measured turbidity currents. *Geology*, **38**, 563–566, https://doi.org/10.1130/G30582.1

Xu, J.P., Noble, M.A. & Rosenfeld, L.K. 2004. In-situ measurements of velocity structure within turbidity currents. *Geophysical Research Letters*, **31**, L09311, https://doi.org/10.1029/2004GL019718